

## NITROGEN PRODUCTION IN STARBURST GALAXIES DETECTED BY GALEX

RYAN P. MALLERY<sup>1</sup>, LISA KEWLEY<sup>2</sup>, R. MICHAEL RICH<sup>1</sup>, SAMIR SALIM<sup>1</sup>, STEPHANE CHARLOT<sup>3,4</sup>, CHRISTY TREMONTI<sup>5</sup>, MARK SEIBERT<sup>6</sup>, TODD SMALL<sup>6</sup>, TED WYDER<sup>6</sup>, TOM A. BARLOW<sup>6</sup>, KARL FORSTER<sup>6</sup>, PETER G. FRIEDMAN<sup>6</sup>, D. CHRISTOPHER MARTIN<sup>6</sup>, PATRICK MORRISSEY<sup>6</sup>, SUSAN G. NEFF<sup>7</sup>, DAVID SCHIMINOVICH<sup>8</sup>, LUCIANA BIANCHI<sup>9</sup>, JOSE DONAS<sup>11</sup>, TIMOTHY M. HECKMAN<sup>12</sup>, YOUNG-WOOK LEE<sup>10</sup>, BARRY F. MADORE<sup>14</sup>, BRUNO MILLIARD<sup>11</sup>, ALEX S. SZALAY<sup>12</sup>, BARRY Y. WELSH<sup>13</sup>, SUK YOUNG YI<sup>10</sup>

*Draft version October 30, 2018*

### ABSTRACT

We investigate the production of nitrogen in star forming galaxies with ultraviolet (UV) radiation detected by the Galaxy Evolution Explorer Satellite (*GALEX*). We use a sample of 8,745 *GALEX* emission line galaxies matched to the Sloan Digital Sky Survey (SDSS) spectroscopic sample. We derive both gas-phase oxygen and nitrogen abundances for the sample, and apply stellar population synthesis models to derive stellar masses and star formation histories of the galaxies. We compare oxygen abundances derived using three different diagnostics. We derive the specific star formation rates of the galaxies by modeling the 7-band *GALEX*+SDSS photometry. We find that galaxies that have  $\log \text{SFR}/M_* \gtrsim -10.0$  typically have values of  $\log \text{N/O} \sim 0.05$  dex less than galaxies with  $\log \text{SFR}/M_* \lesssim -10.0$  and similar oxygen abundances.

*Subject headings:* galaxies: abundances - galaxies: fundamental parameters - galaxies: starburst - ultraviolet: galaxies

### 1. INTRODUCTION

The abundance of nitrogen in galaxies and the site of its creation is critical for our understanding of galaxy chemical evolution. The ratio of N/O is especially useful because both of these elements are created by different mechanisms in different ranges of stellar mass. Nitrogen is produced during hydrogen burning via the CNO and CN cycles, and is created as both a primary and secondary element. In primary nucleosynthesis the production of nitrogen is independent of the initial metallicity of the star. Primary production of nitrogen occurs predominantly only in intermediate mass stars ( $4 \leq M/M_\odot \leq 8$ ) (Matteucci & Tosi 1985; Matteucci 1986) where the nitrogen is produced during hydrogen shell burn-

ing while carbon and oxygen, which are assumed to be primary nucleosynthesis elements, are moved from the core to the outer stellar layers during dredge-up episodes. Recent stellar models that include rotational effects indicate that massive stars between 9 and 20  $M_\odot$  may produce primary nitrogen (Maeder 2000). These massive star models incorporate a convective helium burning shell that penetrates into the hydrogen burning shell, creating primary nitrogen. The discovery of metal-poor halo stars with high N/O ratios by Spite et al. (2005) and Israelian et al. (2004) seems to confirm the primary production of nitrogen in massive stars with a yield that depends on stellar mass and metallicity (Chaippini, Matteuci, & Ballero 2005; Chaippini et al. 2005). In secondary production, nitrogen is synthesized from the carbon and oxygen initially present in the star and its abundance is therefore proportional to the initial heavy element abundance. Secondary production is common to stars of all masses (Matteucci & Tosi 1985; Matteucci 1986). Though the synthesis of nitrogen in stars is becoming better understood, our understanding of the abundance of nitrogen in galaxies is lacking. One way to investigate the primary versus secondary origin of nitrogen is to examine the ratio of N/O as a function of O/H. These abundance ratios are commonly computed from optical nebular emission lines of HII regions (see §5). In the case of primary nucleosynthesis N/O will be constant; secondary enrichment produces a linear correlation between  $\log \text{N/O}$  and  $\log \text{O/H}$ . The combination of primary and secondary nucleosynthesis produces a non-linear relation (see Fig. 3). The abundance ratios of many other elements such as neon, sulfur, and iron with respect to oxygen have been found to tightly correlate with O/H (Izotov et al. 2006), yet at fixed O/H galaxies have been found to have a scatter in N/O of a factor of 2 (Vila-Costas & Edmunds 1993). Until recently, this problem could not be adequately addressed due to small sample sizes, and uncertain abundances.

<sup>1</sup> Department of Physics and Astronomy, University of California, Los Angeles, CA 90095-1562

<sup>2</sup> Institute for Astronomy, University of Hawaii, Honolulu, HI, 4234092309239805

<sup>3</sup> Max-Planck Institut für Astrophysik, D-85748 Garching, Germany

<sup>4</sup> Institut d'Astrophysique de Paris, CNRS, 98 bis boulevard Arago, F-75014 Paris, France

<sup>5</sup> Steward Observatory, 933 North Cherry Avenue, Tucson, AZ 85721

<sup>6</sup> California Institute of Technology, MC 405-47, 1200 East California Boulevard, Pasadena, CA 91125

<sup>7</sup> Laboratory for Astronomy and Solar Physics, NASA Goddard Space Flight Center, Greenbelt, MD 20771

<sup>8</sup> Department of Astronomy, Columbia University, New York, NY 10027

<sup>9</sup> Center for Astrophysical Sciences, The Johns Hopkins University, 3400 N. Charles St., Baltimore, MD 21218

<sup>10</sup> Center for Space Astrophysics, Yonsei University, Seoul 120-749, Korea

<sup>11</sup> Laboratoire d'Astrophysique de Marseille, BP 8, Traverse du Siphon, 13376 Marseille Cedex 12, France

<sup>12</sup> Department of Physics and Astronomy, The Johns Hopkins University, Homewood Campus, Baltimore, MD 21218

<sup>13</sup> Space Sciences Laboratory, University of California at Berkeley, 601 Campbell Hall, Berkeley, CA 94720

<sup>14</sup> Observatories of the Carnegie Institution of Washington, 813 Santa Barbara St., Pasadena, CA 91101

Chemical evolution scenarios proposed to explain this scatter include (1) a primary plus secondary origin of nitrogen but with variable initial mass functions (IMFs) (Alloin et al. 1979), (2) a primary plus secondary origin but with a time delay between the release of nitrogen and the release of oxygen back into the interstellar medium (ISM) (Vila-Costas & Edmunds 1993; Garnett 1990; Thurston, Edmunds & Henry 1996). With regards to the former scenario, Chiappini, Matteucci & Padoan (2000) have found that an IMF constant in space and time better reproduces the observational constraints of the solar neighborhood (i.e. the ratio of metal-poor to metal-rich stars, the ratio of SN II to SN I, and the ratio of He to metal abundance.). Chiappini, Matteucci & Padoan (2000) find that such an IMF also helps reproduce the observed abundance gradient of the Galactic disk more reliably than models with IMFs that depend on metallicity or SFR. In the time delay chemical evolution model, oxygen is released in the supernovae of short lived massive stars. As the metallicity of successive generations of massive stars increases, secondary nitrogen is also released, and then the bulk of nitrogen is released much later in intermediate mass stars. The chemical evolution models of Fields & Olive (1998) for blue compact galaxies and Chiappini, Romano, & Matteucci (2003) for dwarf galaxies, incorporating the variation of stellar yields with stellar mass and stellar evolution timescales, have shown that the scatter in N/O could be reproduced by varying star formation histories.

Work by Considère et al. (2000) on abundances in barred spiral galaxies indicates that the nitrogen abundance is the result of both primary and secondary nucleosynthesis. However, nitrogen abundances taken from a small UV selected galaxy sample detected by FOCA<sup>15</sup> (Contini et al. 2002) show mostly a secondary component, but still with considerable scatter. They proposed that the difference between the two results arises because there is a time delay between the release of oxygen and nitrogen. The UV galaxies were starbursts; consequently, the high mass stars formed during the starburst had released newly synthesized oxygen into the ISM. This increased the oxygen abundance and lowered the N/O ratio of these galaxies such that their new nitrogen and oxygen abundances were consistent with only a secondary nitrogen component. Then later, once the intermediate mass stars formed during the burst have had time to evolve, nitrogen will be released into the ISM. This would increase the nitrogen in these UV galaxies to a similar amount of N/O as the sample of Considère et al. (2000).

The time delay scenario, as stated by Contini et al. (2002), may be oversimplified. It does not account for galaxies that have star formation histories differing from cycles of bursting phases followed by quiescent phases, and was made prior to any evidence for the production of primary nitrogen in massive stars (Maeder 2000; Spite et al. 2005; Chaippini, Matteucci, & Ballero 2005; Chaippini et al. 2005). A more accurate statement is: the release of material by a star of mass,  $M$  into the ISM will cause the N/O ratio of the ISM to increase if its relative yield of  $p_N/p_O$  is greater than 1 and decrease if its

relative yield is less than 1. The new nitrogen and oxygen stellar yields of Chaippini et al. (2005) still indicate that while massive stars ( $M_* > 9M_\odot$ ) produce primary nitrogen, the ratio of nitrogen to oxygen yields for massive stars is  $\lesssim 1$  and still decreases with increasing mass. Thus, a burst of star formation will still initially cause a decrease in N/O, the effect of the new yields only diminishes the extent to which a starburst can conceivably lower N/O. All that is required for the N/O of a galaxy to increase is that its current SFR is less than its past average SFR such that comparatively fewer high mass stars are being formed, allowing for intermediate mass stars of previous generations to dominate the chemical enrichment of the galaxy.

The large amount of uniformly calibrated data from the Sloan Digital Sky Survey (SDSS) has recently enabled robust statistical studies of chemical enrichment (Tremonti et al. 2004). Recently, Izotov et al. (2006) examined the ratio of N/O in metal-poor galaxies,  $12 + \log O/H < 8.5$ , in SDSS DR3 and concluded that the N/O ratio increases with increasing starburst age (decreasing  $EW_{H\beta}$ ) for metal-poor galaxies, due to the ejection of nitrogen by Wolf-Rayet stars. Liang et al (2006) consider a  $\sim 30,000$  galaxy SDSS DR2 sample, and show that objects with higher N/O tend to have lower  $EW_{H\alpha}$ . This result is consistent with those galaxies with current star formation rates that are high with respect to their past average star formation rate, exhibiting a higher oxygen abundance. The oxygen is presumably contributed by the recently formed massive stars. Here we examine the N/O ratio as a function of O/H in a sample of UV selected galaxies detected by the Galaxy Evolution Explorer (GALEX), exploiting the overlap between the GALEX Medium Imaging Survey and the SDSS spectroscopic footprint in the local universe ( $z < 0.3$ ). The large volume of data available from GALEX+SDSS makes it possible to go beyond equivalent widths and calculate physical quantities like stellar masses,  $M_*$ , and specific star formation rates,  $SFR/M_*$ , which can be more easily compared with models when investigating chemical enrichment. We use the  $SFR/M_*$  and  $M_*$ , of these galaxies derived from their 7-band UV-optical photometry (Salim et al. 2008) to test whether the star formation history of a galaxy can explain the observed relationship between the nitrogen and oxygen abundances in our sample and investigate the accuracy of determined abundances. We note that O/H is not equivalent to a time axis, and the values of N/O and O/H represent the current chemical evolutionary stages for galaxies that have most likely had different histories of star formation and other dynamical processes such as galactic winds and gas accretion timescales (Chiappini, Romano, & Matteucci 2003; Diaz & Tosi 1986; Matteucci & Tosi 1985). We expect, nevertheless, that if the time delay scenario is correct, that galaxies currently exhibiting a strong burst of star formation will on average have lower values of N/O than non-bursting galaxies at similar metallicities.

The outline of the paper is as follows. In §2 we describe the data and sources used in this analysis. We present our galaxy sample containing matched GALEX and SDSS sources in §3. An explanation of the derivation of galaxy parameters by matching the models of Bruzual & Charlot (2003) to the 7 color UV-optical SED of each source is given in §4. We describe and con-

<sup>15</sup> FOCA was a balloon-borne 40 cm telescope that imaged at 2015Å, FWHM 188Å (Milliard et l. 1992).

trast the various methods used in determining oxygen abundances in §5 and nitrogen in §6. In §7 we examine the relationship of nitrogen to oxygen for our sample and in §8 we give our conclusions. We assume  $H_0=70 \text{ km s}^{-1} \text{ Mpc}^{-1}$ ,  $\Omega_m=0.3$ , and  $\Omega_\Lambda=0.7$ .

## 2. DATA

We consider galaxies with GALEX photometry from the Medium Imaging Survey (MIS) Internal Release 1.1 (IR1.1),  $m_{lim}(AB) \approx 23$ , and SDSS photometry and spectra. GALEX is a NASA Small Explorer Mission that aims to survey the UV emission from Galactic and extragalactic sources from a 700km circular orbit (Martin et al. 2008; Morrissey et al. 2008). GALEX images the sky simultaneously in two bands, the far-UV (FUV 1344-1786Å) and the near-UV (NUV 1771-2831 Å). Each GALEX circular field is 1.25 deg. in diameter. We use FUV and NUV magnitudes and magnitude errors derived in elliptical apertures<sup>16</sup>.

We use optical photometry for our objects obtained from SDSS Data Release 4 (DR4) spectroscopic sample. Most of our objects were taken from the main galaxy spectroscopic survey ( $r_{lim} < 17.8$ ), but many of our objects were originally targeted as quasars and taken from the quasar spectroscopic survey ( $r_{lim} < 19.5$  York et al. (2000)). The SDSS photometric data are taken with the 2.5m telescope at Apache Point Observatory. Imaging is obtained in *ugriz* bands (Fukugita et al. 1996; Smith et al. 2002). The imaging data are photometrically (Hogg et al. 2001) and astrometrically (Pier et al. 2003) calibrated. An overview of the SDSS data pipelines and products can be found in Stoughton et al. (2002).

The SDSS spectra are acquired using 3" diameter fibers positioned on the centers of the target galaxies. The spectra are flux and wavelength calibrated for wavelengths between 3800-9200Å at resolving power (York et al. 2000)  $R \equiv \lambda/\Delta\lambda = 1850-2200$ . We use continuum subtracted emission-line fluxes and flux errors from the SDSS spectra measured by Tremonti et al. (2004), to divide and classify the sample in terms of emission-line ratios, and to derive nebular abundances.

## 3. THE SAMPLE

We use a sample constructed by matching objects with GALEX MIS IR1.1 detections to galaxies in the SDSS DR4 spectroscopic sample. The objects are matched within a 4" radius (Seibert et al. 2005; Salim et al. 2008). We accept only unique matches and discard objects that contain multiple matches. We restrict the sample to galaxies with  $z < 0.3$  that are detected by GALEX in the NUV at a  $3\sigma$  level. We further restrict the sample to galaxies with spectral *r*-band fluxes greater than 20% of their total *r*-band fluxes. Kewley, Jansen & Geller (2005) found that in samples where the spectroscopic fiber collects greater than 20% of the galaxy light, the fiber metallicities approximate global values. This criterion gives a sample of 36225 objects.

In order to constrain the errors on the derived abundances for objects, we impose detection criteria for several emission lines. We remove galaxies with  $< 5\sigma$  detections of the Balmer lines  $H\alpha$  and  $H\beta$  and  $[NII]\lambda 6584$ .

For other oxygen forbidden lines that are used in the analysis,  $[OII]\lambda 3726, 3729$   $[OIII]\lambda 5007$ , we remove galaxies with  $< 3\sigma$  detections. We note that demanding a  $[OII]$  detection restricts the galaxy's redshift to  $z > 0.03$  due to the wavelength cutoff of the SDSS spectrograph at 3800Å. These constraints trim the sample to 12213 galaxies.

We identify Active Galactic Nuclei (AGN) in our sample by using the line diagnostic diagram  $[NII]/H\alpha$  versus  $[OIII]/H\beta$  (Baldwin, Phillips, & Terlevich 1981). We use the formula of Kauffmann et al. (2003b) to remove galaxies with contributions to their emission line spectrum from AGN. The fraction of galaxies removed because of possible contamination due to AGN is  $\sim 21\%$ .

Other sources of emission-line flux besides star forming regions include planetary nebulae (PN), and supernova remnants (SNR). Studies by Oey et al. (2000) of the Large Magellanic Cloud (LMC) show that SNRs affect the emission-line spectra at a fairly low level. As discussed in Charlot & Longhetti (2000) the radiation from planetary nebulae can be neglected since the ionizing radiation is typically less than 0.1 percent of that produced by massive stars at an earlier age.

We finally remove 831 galaxies with failed fits to the photometric 7-band SED that give reduced  $\chi^2 > 10$ . This gives a sample of 8,745 galaxies, from which 72% are from the SDSS main galaxy sample. Galaxies in the final star forming sample with  $3\sigma$  FUV detections comprise  $\sim 84\%$  of the sample. The emission-line criteria we use selects galaxies that are blue in  $NUV-r$ , with  $NUV-r < 4$ . GALEX is remarkably sensitive to star-forming galaxies. In all of the GALEX MIS IR1.1 fields only 155 galaxies that are detected in SDSS DR4 and that satisfy our emission line criteria do not have  $3\sigma$  NUV or FUV detections. The percent GALEX detection is 99.4% for  $r < 17.8$  and 97.9% for  $r > 17.8$ .

## 4. DERIVED GALAXY PARAMETERS

We use the following galaxy parameters derived by Salim et al. (2008): the NUV and FUV dust attenuation,  $A_{NUV}$  and  $A_{FUV}$  in magnitudes, the current star formation rate, SFR, averaged over the past 100 Myr in  $M_\odot \text{ yr}^{-1}$ , the present-day stellar mass,  $M_*$ , of the galaxy in  $M_\odot$ , the specific star formation rate,  $SFR/M_*$ , and the fraction of stellar mass formed in starbursts over the last 100Myr,  $F_{Burst}$ . Galaxy parameters are derived from model libraries of galaxies at redshifts of .05, .10, .15, .20, and .25. Each library consists of  $\sim 10^5$  models. Each model is defined by several parameters: galaxy age, optical depth, star formation history, and metallicity. The star formation history of each model follows the prescription of Kauffmann et al. (2003a) and consists of an underlying, continuous, exponentially declining SFR upon which bursts of star formation, random in time and amplitude, are superimposed. Dust attenuation in each model is parametrized using the prescription of Charlot & Fall (2000). A description of the prior distributions of the model parameters is discussed in Salim et al. (2005) and Salim et al. (2008).

Model spectral energy distributions (SEDs) are created for each set of model parameters using the population synthesis code of Bruzual & Charlot (2003) and assuming a Kroupa (2001) IMF. The model SEDs are convolved with the GALEX and SDSS filter response

<sup>16</sup> GALEX source detection and measurement is obtained from SExtractor (Bertin, & Arnouts 1996)

curves. Statistical estimates of physical galaxy parameters are derived by comparing the observed 7 band GALEX/SDSS fluxes of each galaxy to all the convolved model SEDs in the nearest redshift library. Probability density functions (PDFs) for each physical parameter are created by assigning weights to the parameters of a model. The  $\chi^2$  goodness of fit of each model determines the weight ( $\propto \exp[-\chi^2/2]$ ) that is assigned to the parameters of that model. The median of the PDF is taken as the estimate of the galaxy parameter. An estimate of the error for the parameters is taken as 1/4 of the 2.5-97.5 percentile range. Table 1 lists the parameters and their mean errors.

## 5. OXYGEN ABUNDANCE

In order to estimate the abundance of oxygen we employ three methods using relations of various emission-line fluxes: the  $R_{23}$  strong-line abundance calibration of McGaugh (1991), the O3N2 strong-line calibration of Pettini & Pagel (2004) and the Bayesian metallicity estimates of Tremonti et al. (2004).

We use the following flux ratios in our calculations dereddened using the extinction curve of Seaton (1979), assuming  $R_v = 3.1$  and Case B recombination (Osterbrock 1989):

$$\frac{[OIII]}{[OII]} \equiv \frac{[OIII]\lambda 5007}{[OII]\lambda 3727} \quad (1)$$

$$O_{32} \equiv \frac{[OIII]\lambda 5007 + [OIII]\lambda 4959}{[OII]\lambda 3727} \quad (2)$$

$$\frac{[OIII]}{H\beta} \equiv \frac{[OIII]\lambda 5007}{H\beta} \quad (3)$$

$$\frac{[NII]}{H\alpha} \equiv \frac{[NII]\lambda 6584}{H\alpha} \quad (4)$$

$$\frac{[NII]}{[OII]} \equiv \frac{[NII]\lambda 6584}{[OII]\lambda 3727} \quad (5)$$

$$R_{23} \equiv \frac{[OII]\lambda 3727 + [OIII]\lambda 5007 + [OIII]\lambda 4959}{H\beta} \quad (6)$$

$$O3N2 \equiv \log\left(\frac{[OIII]\lambda 5007/H\beta}{[NII]\lambda 6583/H\alpha}\right) \quad (7)$$

The strong line abundance calibration was first developed by Pagel et al. (1979) and Alloin et al. (1979). The various line ratios that have been used to calculate abundances are  $[NII]/H\alpha$ ,  $[OIII]/[NII]$ ,  $[NII]/[OII]$ ,  $([SII] \lambda\lambda 6671, 6731 + [SIII] \lambda\lambda 9069, 9532)/H\beta$ , and  $R_{23}$ , which was first introduced by Pagel et al. (1979). Oxygen strong line abundance calibrations are either (1) based on photo-ionization models (Diaz et al. 2000; Kewley & Dopita 2002) or (2) on abundances measured in nearby HII regions where the electron temperatures of the ionized regions can be measured. The latter method requires detection of faint auroral emission lines (e.g.,  $[OIII]\lambda 4363$ ,  $[NII]\lambda 5755$ ) to determine the electron temperature,  $T_e$ . The empirical strong-line analytical expressions are created from these measurements to estimate the abundance in galaxies and HII regions that lack significant detections of the auroral lines but have similar abundances.

Recently the studies of Kennicutt, Bresolin & Garnett (2003); Bresolin, Garnett, & Kennicutt (2004); Garnett, Kennicutt & Bresolin (2004) using electron temperatures for high metallicity HII regions in M101 and M51, indicate that various strong-line methods calibrated to photo-ionization models (e.g. McGaugh (1991)) estimate a higher abundance at high metallicities by 0.2-0.5 dex than the  $T_e$  method abundances. It is currently not clear which method is correct. There is some evidence that the abundances calculated by the  $T_e$  method may be underestimated due to temperature fluctuations in the ionized regions causing the electron temperatures to be overestimated, and that the strong line abundances may be more correct since their line ratios are not as temperature sensitive as  $[OIII]\lambda 4363$  (Peimbert et al 2006; Bresolin 2006; Bresolin, Garnett, & Kennicutt 2004; Kennicutt, Bresolin & Garnett 2003).

In our analysis we use two strong-line calibrations to estimate the oxygen abundance: the  $R_{23}$  diagnostic of McGaugh (1991) calibrated from photo-ionization models, and the strong-line ( $[OIII]/H\beta$ )/( $[NII]/H\alpha$ ) diagnostic of Pettini & Pagel (2004) calibrated from  $T_e$  abundances. The derived abundances for each method are respectively labeled M91, and O3N2 throughout the remainder of this work. We add to these strong line abundances the strong line oxygen abundance estimates of Tremonti et al. (2004) (hereafter labeled T04), obtained from likelihood distributions of oxygen abundances derived by matching emission line fluxes from integrated galaxy spectra models of Charlot & Longhetti (2000) to the measured fluxes.

The  $R_{23}$  analytical expressions calibrated by McGaugh (1991) and given in Kobulnicky, Kennicutt, & Pizagno (1999) that we use to calculate M91 are cited below. Many other authors have developed techniques for estimating abundances from  $R_{23}$ . Examples include Charlot & Longhetti (2000), Alloin et al. (1979), and Edmunds & Pagel (1984).  $R_{23}$  is useful because it provides an estimate of the total cooling due to oxygen. The major caveat with  $R_{23}$  is that it is double valued with respect to metallicity. At low oxygen abundances,  $12 + \log O/H \lesssim 8.4$ ,  $R_{23}$  increases with rising abundance until  $12 + \log O/H \gtrsim 8.4$ , after which it begins to decrease as metals begin to cause efficient cooling, lowering the electron temperature and thus decreasing the amount of collisional excitation of the oxygen ions. The metal-poor branch expression is:

$$12 + \log(O/H) = 7.065 + .767x + .602x^2 - y(.29 + .332x - .3318x^2) \quad (8)$$

and the metal-rich branch expression is:

$$12 + \log(O/H) = 9.061 - .2x - .237x^2 - .305x^3 - .0283x^4 - y(.0047 - .022x) \quad (9)$$

where  $x \equiv \log(R_{23})$  and  $y \equiv \log(O_{32})$ .  $O_{32}$  is used to correct the effect of the ionization parameter on  $R_{23}$ . Kewley & Dopita (2002) have found that the  $O_{32}$  ratio depends on metallicity and as a result is not a good indicator of ionization unless an initial estimate of metallicity can be given and an iterative process is applied.

To determine on which branch the correct solution

lies, we use the metallicity sensitive ratios  $[\text{NII}]/\text{H}\alpha$  and  $[\text{NII}]/[\text{OII}]$ . For  $\log([\text{NII}]/\text{H}\alpha) < -1$  and  $\log([\text{NII}]/[\text{OII}]) < -1.5$  we use the metal-poor expression. For  $\log([\text{NII}]/\text{H}\alpha) > -1$  and  $\log([\text{NII}]/[\text{OII}]) > -0.8$  we use the metal-rich expression. If  $-0.8 > \log([\text{NII}]/[\text{OII}]) > -1.5$ , then we use the  $\log([\text{NII}]/\text{H}\alpha)$  ratio as stated above to determine the correct branch. Where the two ratios give conflicting estimates, the average of the two expressions is used to derive the abundance. This is because the solutions for the two branches converge at intermediate metallicities,  $12 + \log O/H \sim 8.4$ , and it is near this metallicity where the metallicity sensitive ratios are likely to give a conflicting answer. The average of the two branch solutions in this case should minimize any bias in the calculations. A caveat with this procedure is that galaxies with intermediate oxygen abundances but with high SFRs will have lower ratios of  $[\text{NII}]/\text{H}\alpha$  and as a result can have their abundances calculated with the lower branch and therefore underestimated.

The strong line calibration O3N2 developed by Pettini & Pagel (2004) is shown below. The calibration based on this flux ratio also has several problems. First, it is not corrected for ionization parameter. Second, it is based on the flux from a forbidden nitrogen line whose abundance many authors claim depends star-formation history of the galaxy. As a result the calibration is accurate to  $\log(O/H) = \pm 0.25$ , and is only valid for  $\text{O3N2} < 1.9$  (e.g.  $12 + \log(O/H) \gtrsim 8.1$ ).

$$12 + \log(O/H) = 8.73 - 0.32 \times \text{O3N2} \quad (10)$$

There is also evidence that at metallicities  $\gtrsim \log(O/H)_\odot$  ( $\text{O3N2} \lesssim 0.4$ ) the O3N2 calibration overestimates the oxygen abundance (Bresolin, Garnett, & Kennicutt 2004).

Figure 1 shows the difference between all the abundance calibrations as a function of stellar mass. In the figure we have transformed each panel into a 75 by 75 pixel image. The mean SFR/ $M_*$  of the points in each pixel is shown in true color representation. The mean difference between M91 and O3N2 shows some dependence on stellar mass, with the lower branch of M91 giving lower abundances than O3N2, typically about 0.1 dex with a dispersion of 0.18 dex. The upper branch of M91 calculates larger abundances than O3N2 typically by  $\sim 0.2$  dex with a dispersion of 0.14 dex. While the offset between O3N2 and M91 shows little dependence on stellar mass, the offset between T04, and the M91, O3N2 diagnostics show a dependence on stellar mass. As galaxy mass increases, T04 estimates an increasingly larger metallicity than the other two calibrations.

## 6. NITROGEN ABUNDANCE

We calculate nitrogen abundance estimates by first using the calibration of Thurston, Edmunds & Henry (1996) to estimate the temperature in the  $[\text{NII}]$  emission region using their calibrated empirical relation created from photo-ionization models:

$$t_{[\text{NII}]} = 0.6065 + 0.1600x + 0.1878x^2 + 0.2803x^3 \quad (11)$$

where  $x \equiv \log R_{23}$ . We then use this temperature to determine the the ratio of  $\text{N}^+/\text{O}^+$  based on the empirical calibration of Pagel et al. (1992) based off of  $T_e$  abundances:

$$\text{Log} \frac{\text{N}^+}{\text{O}^+} = \text{Log} \frac{[\text{NII}]}{[\text{OII}]} + .307 - .02 \text{Log} t_{[\text{NII}]} - \frac{0.726}{t_{[\text{NII}]}} \quad (12)$$

We finally assume that  $\text{N}/\text{O} = \text{N}^+/\text{O}^+$ . Thurston, Edmunds & Henry (1996) found through modeling that this assumption is reliable, with only small uncertainties,  $\sim .05$  dex. Garnett (1990) concurs that the  $\text{N}^+/\text{O}^+$  is an accurate  $\text{N}/\text{O}$  indicator for low abundances or where the ionizing stars are hotter than 40,000K. Results of modeling by Stasinka (1990) show that even at high abundance, equating the ion ratio to the element ratio is good to within 5%.

We also calculate the nitrogen and oxygen abundance via the  $T_e$  method for the 33 objects in our *GALEX* emission line sample having at least a  $3\sigma$  detection of  $[\text{OIII}]43643$  to ensure reliable estimates of the electron temperature in the  $[\text{OIII}]$  ionization regions. Table 2 shows the derived  $T_e$  abundances and derived galaxy parameters from SED fitting for these objects. We use the TEMDEN procedure in the IRAF package Nebular (Shaw & Dufour 1995) to derive the electron temperature from the ratio of  $([\text{OIII}]5007 + [\text{OIII}]4959)/[\text{OIII}]4363$ . The electron temperature in the  $[\text{OII}]$  and  $[\text{NII}]$  regions were then estimated using the linear relation from Garnett (1992) to convert the mean  $[\text{OIII}]$  electron temperatures into mean electron temperatures in the  $[\text{OII}]$  ionization regions. We then assume that since  $[\text{NII}]$  and  $[\text{OII}]$  have relatively similar ionization energies that the  $[\text{NII}]$  electron temperature equals the  $[\text{OII}]$  electron temperature. The abundance of each ion  $\text{O}^{2+}$ ,  $\text{O}^+$ , and  $\text{N}^+$  were then calculated using the IONIC procedure in Nebular.

All four oxygen calculations show a small abundance range for this sub-sample of objects, thus limiting our ability to determine if the difference between the two methods has any dependence on abundance or on  $\text{N}/\text{O}$ . The  $\text{N}/\text{O}$  ratio calculated with the strong line calibration shows that it is typically  $\sim 0.1$  dex greater than the ratio determined by the  $T_e$  method with a dispersion of 0.07 dex. How accurate the strong line  $\text{N}/\text{O}$  ratio is for higher oxygen abundances is unknown, and its precision is lacking. The mean error on  $\log \text{N}/\text{O}$  for the entire sample is 0.17 dex, due mostly to the error on the  $R_{23}$  temperature. For the the purposes of the rest of our analysis, the accuracy of the strong line nitrogen diagnostic does not matter, only the relative difference between each galaxy is of importance.

## 7. THE $\text{N}/\text{O}$ VERSUS $\text{O}/\text{H}$ RELATIONSHIP

The time delay scenario for the production of nitrogen predicts that starbursting galaxies exhibit a rise in oxygen abundance along with a drop in  $\text{N}/\text{O}$  (Contini et al. 2002; van Zee & Haynes 2006; Henry & Worthey 1999). The addition of UV data from *GALEX* to the 5 band SDSS photometry makes it possible to distinguish between galaxies recently hosting starbursts and those with declining star formation, because the FUV passband is responsive to star formation on timescales of 10 Myr and the NUV passband on timescales of 100 Myr (Martin et al. 2008; Bruzual & Charlot 2003). We use our  $\text{O}/\text{H}$  and  $\text{N}/\text{O}$  estimates along with the results from the Bayesian broad

band SED analysis to examine if the relative abundance of nitrogen to oxygen in a galaxy can be explained by the galaxy’s star formation history.

The relationship between N/O and O/H for our sample is shown in Figure 2. The points have been pixelated and then scaled by color to show the mean value of specific star formation rate of the points in each pixel. The specific star formation rate indicates the relative number of recently formed ( $\sim 100 Myr$ ) high mass stars to the cumulative number of stars formed over a galaxy’s star formation history. Galaxies with large specific star formation rates have recently undergone a burst of star formation or have a slowly declining SFR. The mean standard deviation in  $SFR/M_*$  for each pixel is  $\sim 0.07$  dex. In Figure 3 we plot our nitrogen-oxygen relationship again with the data points plotted as a shaded 2D histogram to aid the interpretation of the previous figure.

In the figures we have included the simple closed box model of Vila-Costas & Edmunds (1993) for the primary (solid line), secondary (dashed line), and primary + secondary (dashed-dotted line) production of nitrogen. This model assumes that nitrogen has both a primary and secondary component, and that oxygen has only a primary component. The time rate of change of each element is taken to be proportional to the star formation rate which is assumed to equal a constant times the fraction of galaxy’s mass in gas ( $= 1$  at  $t=0$ ). Assuming that there are no time delays in the release of the material, a solution for the model can be found,  $\log[N/O] = \log[a + b \times [O/H]]$ , where  $a$  is the primary yield of nitrogen divided by the yield of oxygen and  $b$  is the secondary yield of nitrogen divided by the yield of oxygen. Vila-Costas & Edmunds (1993) quote values of  $a=.034$  and  $b=120$  using a by-eye fit to line strengths taken from literature for HII regions in nearby galaxies.

The three oxygen abundance methods, allowing for the relative offsets between each method, are all consistent with galaxies containing primary nitrogen at low metallicities and a secondary component at higher metallicities. The mean scatter of N/O as a function of oxygen abundance is 0.08 dex for O3N2, 0.11 dex for M91 and 0.13 dex for T04. We note that these three derivations for oxygen abundance are not completely independent of the nitrogen abundance. The O3N2 value depends on a flux ratio containing [NII]6584, while  $R_{23}$  is used to calculate the [NII] temperature required to determine the N/O ratio. Furthermore, the models used to derive T04 have prior distributions of metallicities where nitrogen abundance is selected to have a only a primary dependence on the oxygen abundance below  $12 + \log O/H < 8.25$ , and a completely secondary dependence for metallicities greater than this. T04 and O3N2 diagnostics are therefore predetermined to exhibit secondary nitrogen production, and are not useful in determining the relative amount of secondary or primary nitrogen in each galaxy. Furthermore, the abundances determined by T04 may slightly overestimate abundances for galaxies that have an increased N/O ratio from primary+secondary nitrogen. The likelihood estimates of T04 depend on the flux from nitrogen emission lines, but only consider that nitrogen is secondary in origin, and do not accurately account for nitrogen fluxes from galaxies containing secondary plus primary nitrogen. Of the three diagnostics, the M91 calculation has the least dependence on the N/O

diagnostic. This is because the N/O calculation depends slightly on the temperature estimate obtained by  $R_{23}$ , which introduces a scatter in N/O that increases from  $\sim 0.04$  dex at the lowest values of N/O to  $\sim 0.1$  dex at highest N/O values. The fact that O3N2 and T04 show a similar secondary dependence on N/O as M91 is an indication that the interdependence between the N/O calculation and T04 or O3N2 is only a small effect.

### 7.1. N/O and $SFR/M_*$

The main results emerge when we consider the relationship between N/O and O/H as a function of specific star formation rate. Figure 2 gives several interesting results. First, for galaxies with high abundances ( $12 + \log O/H \gtrsim 8.6$ ), the M91 and T04 diagnostics both indicate that for galaxies with similar O/H, the most extreme starbursts (highest values of  $SFR/M_*$ ) tend to have lower N/O. This is shown more clearly in Figures 3 and 4. In these figures we divide our emission sample into sub-samples of specific star formation rate:  $\log SFR/M_* < -10.1$  (red points),  $-10.1 < \log SFR/M_* < -9.1$  (green points), and  $\log SFR/M_* > -9.1$  (blue points). We then calculate the mean N/O value and error on the mean for each of the sub-samples in increments of 0.1 dex in  $\log O/H$ . Figure 3 plots the mean N/O values for each sub-sample as a function of metallicity, and figure 4 plots the difference between the mean N/O value in each sub-sample and the mean N/O value for the entire sample. Tables 3, 4 and 5 list the mean values of N/O, the errors on the mean, and the number of galaxies for each bin of O/H with more than 30 galaxies in each sub-sample. All three diagnostics show that the galaxies with  $\log SFR/M_* > -10.1$  have lower N/O values than galaxies in the lowest specific star formation rate sub-sample ( $\log SFR/M_* < -10.1$ ) in each decrement of metallicity between 8.5 and 9.0 dex. As metallicity increases, and nitrogen becomes largely secondary in origin, and the difference between the N/O ratios of the sub-sample with the lowest specific star formation rates and the other two sub-samples decreases.

The M91 and T04 diagnostics also show that the most extreme starbursts ( $\log SFR/M_* > -9.1$ ) at intermediate metallicities on average have N/O ratios 0.02 dex lower than galaxies with average specific star formation rates,  $-10.1 < \log SFR/M_* < -9.1$ , a decrease in N/O of  $\sim 3\%$ . The O3N2 diagnostic shows the opposite trend of the other two diagnostics since O3N2 is not corrected for ionization parameter. At the lowest and highest metallicities no difference is found between the N/O ratios of the two sub-samples in all three diagnostics.

Our findings are consistent with similar conclusions reached by Contini et al. (2002). The galaxies with the lower specific star formation rates have the highest N/O ratios because they are currently forming comparatively fewer high mass stars. This allows the chemical enrichment of the galaxy to be dominated by the products of intermediate mass stars, which generate more nitrogen than oxygen, causing N/O in these galaxies to rise. At low metallicities no difference is found between the N/O ratios of the the most extreme starbursts and the average star-forming sub-samples. This is because there are only a small number of galaxies in our sample with low metallicities and most of these are in the sub-sample with the highest specific star formation rates. At

high metallicities, no difference is found between the the most extreme starbursts and the average star-forming sub-sample. This is presumably because the oxygen generated by the high mass stars formed during the latest starburst constitutes only a small fraction of the total oxygen abundance of the galaxy and has little effect on lowering the N/O ratio. At intermediate metallicities the oxygen abundance is relatively small, such that the oxygen created in a starburst constitutes a large fraction of the oxygen abundance of a galaxy and causes a larger decrease in the N/O ratio.

Other possible explanations for the N/O ratios are variable IMFs and galactic winds. An IMF that produces more massive stars for galaxies with higher specific star formation rates, could possibly cause the low N/O ratios of the strongest starbursts seen in Figures 2,3, and 4. Such a variable IMF could plausibly have a slope parametrized by either metallicity, SFR, or both. Silk (1995) conjectures that the IMFs of starbursts may be weighted to form more massive stars, and several authors have previously parametrized IMFs with a dependence on metallicity (Matteucci & Tornambe 1985; Scully et al. 1996). At this time, the validity of a variable IMF and its effect on the abundances cannot be assessed. We find no need to invoke a variable IMF to model the UV and optical SEDs of these galaxies. Furthermore, Chiappini, Matteucci & Padoan (2000) have found that that chemical evolution models for the Galaxy that use a metallicity dependent IMF do not adequately reproduce the observational constraints of the solar neighborhood.

Galaxies with high specific star formation rates could also have galactic winds that differentially remove one element with respect to the other. With regards to differential flow of oxygen, van Zee & Haynes (2006) examined the ratio of N/O for a sample of dwarf galaxies, and argues that their data suggests that either differential outflow of oxygen occurs in every galaxy in their sample with the same efficiency or that differential outflow of oxygen has a negligible effect on N/O ratios. They found that the correlation of oxygen abundance with optical luminosity for their sample had a lower scatter than the correlation of nitrogen abundance with optical luminosity. They argue that if differential outflow was the cause of the scatter in N/O, then the oxygen-luminosity correlation should have a larger scatter than the nitrogen-luminosity correlation, since the the outflow of oxygen would depend on other galaxy parameters such as galaxy mass, and ISM structure. Nitrogen may be differentially removed in galaxies that have high specific star formation rates, but there is no reasonable explanation as to why this might occur. In fact, one would expect the opposite, that oxygen and not nitrogen would be differentially removed in starbursts since the kinetic energy responsible for ejecting the material likely comes from the supernovae of high mass stars that produce very little nitrogen with respect to oxygen.

### 7.2. $N/O$ vs $M_*$ and $g-r$ optical color

In order to further test the above explanation, we plot the nitrogen to oxygen relationship again, with the pixels scaled by color with mean values of stellar mass, and  $g-r$  color in Figures 5 and 6 respectively. Tremonti et al. (2004) found a tight correlation of 0.1 dex between in-

creasing stellar mass and oxygen abundance, so we expect that mass will increase with O/H. Figure 5 shows that the stellar mass increases with O/H with little dependence on N/O for all three methods. Along the same lines, van Zee & Haynes (2006) analyze a dwarf galaxy sample and conclude that a trend of increasing N/O correlates with redder B-V color and hence, lower star formation rate. Based on this result, we expect that increasing values of N/O should correlate with redder  $g-r$  color. In figure 6 we see that as N/O increases the average  $g-r$  color increases for T04, M91, and O3N2 at high metallicities. At metallicities below  $12 + \log O/H \sim 8.4$  both M91, and T04 show this trend. O3N2 does not because it is not corrected for ionization effects. All methods of determining the oxygen abundance show a dependence on mass irrespective of their nitrogen abundance. The T04 and M91 diagnostics show that galaxies of similar metallicity but with higher N/O values have redder  $g-r$  color. These results suggest that the trend between higher specific star formation rates and lower N/O values is a real trend, but more reliable and consistent metallicity diagnostics are required to test this result.

### 7.3. $T_e$ sample $N/O$ vs $O/H$

As a further check, we use the  $T_e$  method abundances to determine whether the trend for galaxies with higher SFR/ $M_*$  to have lower N/O ratios is genuine, and not produced by the strong line abundance calculations themselves due to a dependence on an unknown galaxy parameter. The abundances derived from the  $T_e$  method are dependent only on electron temperature and density, and the N/O ratio calculated by this method is not predetermined to show secondary dependence. In Figure 7 we show the N/O ratio versus O/H for the 33 galaxies with abundances measured by the  $T_e$  method. In the upper left the points are colored by their  $g-r$  optical colors. Even though there is a good deal of scatter in the figure, the galaxies that have the lowest N/O ratios tend to be the bluest in  $g-r$ , with the mean value of  $g-r = 0.12$  and a standard error on the mean of .04 for galaxies with  $\log N/O < -1.5$  and  $g-r = 0.2$  with a standard error on the mean of 0.04 for galaxies with  $\log N/O > -1.5$ . These galaxies also tend to have slightly higher specific star formation rates with a mean difference of 0.12 dex between galaxies with  $\log N/O < -1.5$  and galaxies with  $\log N/O > -1.5$ . The galaxies with lower N/O ratios also have slightly higher  $H\alpha$  equivalent widths, which is an indicator of the current star formation relative to past star formation, on timescales of 10 Myr. The SED fitting indicates that to a 95% reliability at least half of these galaxies formed 1% (and as much as  $\sim 50\%$ ) of their stellar mass in bursts within the last 100Myr. If there is indeed a time delay between the release of oxygen from the massive stars and nitrogen from the intermediate mass stars, then these starburst galaxies should have an influx of newly synthesized oxygen that will raise the oxygen abundance and reduce the N/O ratio. The results from the  $T_e$  abundances slightly favor this scenario, but due to the small sample of galaxies with  $3\sigma$  detections of [OIII]4363, the small range of specific star formation rates, and the uncertainties on the abundances, we are unable to discern if the star formation history is really the cause of the scatter of N/O values for the  $T_e$  sample. We would expect that since all of the 33 galax-

ies are large starbursts, that the N/O ratios would lie close to the secondary nitrogen curve. The explanation posited by Izotov et al. (2006) for the scatter in N/O for galaxies with similar metallicities is that the Wolf Rayet stars in these galaxies have released a significant amount of nitrogen from winds, which being an order of magnitude more dense than the surrounding ISM can cause the N/O ratio to appear high, increasing by as much as 0.23 dex. The N/O ratio will decrease as the nitrogen from the WR winds has time to diffuse into density equilibrium with the ISM, raising the overall ISM log N/O ratio by 0.03 dex. However, the chemical evolution models of Chiappini, Romano, & Matteucci (2003) show that the scatter in N/O ratios of dwarf galaxies at metallicities similar to those in our  $T_e$  sample can be explained by different star formation histories, different burst strengths, and burst durations; they show that there is no need to invoke nitrogen from winds of massive stars to show this effect. The galaxies with  $\log N/O > -1.5$  have on average only slightly bluer optical colors than the rest of the  $T_e$  galaxies. This indicates that intermediate mass stars from the last major star formation event may be responsible for the high N/O ratios, but does not rule out that winds could cause a portion of the observed scatter, (though the errors on the measured abundances are able to account for a large portion of the observed scatter in N/O). To resolve this issue, and effect of variable IMFs or other dynamical processes on N/O such as mixing timescales of the newly synthesized material, more reliable and consistent metallicity measurements are needed, with errors in the derived abundance less than 0.1 dex. New nitrogen diagnostics for metal rich galaxies are particularly needed to compare our results obtained using the Pagel et al. (1992) strong line diagnostic. These results should also be compared to chemical evolution models to substantiate their validity.

## 8. CONCLUSION

We consider galaxies detected by *GALEX* in the Medium Imaging Survey to a limiting magnitude of  $NUV = 23(AB)$ . We match our UV star-forming galaxies to  $z = 0.3$  with the SDSS DR4 spectroscopic sample.

1. *GALEX* at MIS depth ( $NUV_{limit} \sim 23.0AB$ ) detects 98.4% of star forming SDSS galaxies in the DR4 spectroscopic sample matching our emission line criteria of  $5\sigma$  detections of  $H\alpha$ ,  $H\beta$ ,  $[NII]6584$ , and  $3\sigma$  detections of  $[OIII]5007$  and  $[OII]3727$ .

2. For our emission line sample of  $\sim 8,000$  *GALEX*/SDSS star forming galaxies, we have examined each galaxy's oxygen abundance for three strong line abundance measurements. These are calibrated off photo-ionization models, M91,  $T_e$  determined abundances, O3N2, and the Bayesian likelihood estimates, T04. We compare each abundance method as a function of both  $M_*$  and  $SFR/M_*$ . Compared to the other two methods O3N2 is found to increasingly estimate lower oxygen abundances for galaxies with higher  $SFR/M_*$  since it is not corrected for ionization parameter.

3. We investigate the relationship between N/O and O/H using the three different O/H diagnostics and the strong line calculation of N/O from Pagel et al. (1992). We use the specific SFR derived from SED fits to the 7-band *GALEX*+SDSS photometry to indicate of the strength of the starbursts in each galaxy over the last 100Myr.

4. Star forming galaxies that are currently forming a large percentage of their stellar mass, as parametrized by  $SFR/M_*$ , have smaller values of N/O at a given metallicity for for all three metallicity diagnostics, supporting the results of Contini et al. (2002). This trend spans the metallicity range of  $\sim 0.6$  dex from  $12 + \log O/H \sim 8.4$  to  $12 + \log O/H \sim 9.0$  dex and suggests the scenario that the scatter in N/O ratio for galaxies of similar metallicities is due to the ratio of current to past averaged SFR. The observed effect is modest, since the change in N/O is of the order of the abundance uncertainties. However the abundance dispersion could also arise due to varying mixing times of the newly synthesized oxygen into the ISM. More realistic and consistent metallicity diagnostics are required to further test this result.

*GALEX* is a NASA Small Explorer, launched in April 2003. We gratefully acknowledge NASA's support for construction, operation, and science analysis for the *GALEX* mission, developed in cooperation with the CNES of France and the Korean Ministry of Science and Technology. Funding for the creation and distribution of the SDSS Archive has been provided by the Alfred P. Sloan Foundation, the Participating Institutions, NASA, NSF, DoE, Monbukagakusho, and the Max Planck Society.

*Facilities:* *GALEX*

## REFERENCES

- Alloin, D., Collin-Souffrin, S., Joly, M., & Vigroux, L. 1979, *A&A*, 78, 200  
 Baldwin, J. A., Phillips, M. M., & Terlevich, R. 1981, *PASP*, 93, 5  
 Bertin, E., & Arnouts, S. 1996, *A&AS*, 117, 393  
 Bresolin, F. 2006, *astro-ph/0608410*  
 Bresolin, F., Garnett, D. R. & Kennicutt, R. C. 2004, *ApJ*, 615, 228  
 Bruzual, G., & Charlot, S. 2003, *MNRAS*, 344, 1000  
 Chiappini, C., Matteucci, F., & Padoan, P. 2000, *ApJ*, 528, 711  
 Chiappini, C., Romano, D., & Matteucci, F. 2003, *MNRAS*, 339, 63  
 Chiappini, C., Matteucci, F., Ballero, S. K. 2005, *A&A*, 437, 429  
 Chiappini, C., Hirschi, R., Meynet, G., Maeder, A., & Matteucci, F. 2006, *A&A*, 449, 27  
 Charlot, S., & Longhetti 2000, *MNRAS*, 323 887  
 Charlot, S., & Fall, S. M. 2000, *ApJ* 539, 718  
 Considere, S., Coziol, R., Contini, T., & Davoust, E. 2000, *A&A*, 356, 89  
 Contini, T., Treyer, M. A., Sullivan, M., & Ellis, R. S. 2002, *MNRAS*, 330, 75  
 Diaz, A. I., Castellanos, M., Terlevich, E., & Garcia-Vargas, M. L. 2000, *MNRAS*, 318, 462



- Diaz, A. I., & Tosi, M. 1996, *A&A*, 158, 60
- Edmunds, M. G., & Pagel, B. E. J. 1984, *MNRAS*, 211, 507
- Feilds, B. D., & Olive, K. A. 1998, *ApJ*, 516, 797
- Fukugita, M., Ichikawa, T., Gunn, J. E., Doi, M., Shimasaku, K., & Schneider, D. P. 1996, *AJ*, 111, 1748
- Garnett, D. R., Kennicutt, R. C., & Bresolin, F. 2004, *ApJ*, 607, 21
- Garnett, D. R. 1990, *AJ*, 363, 142
- Henry, R. B. C., & Worthey, G. 1999, *PASP*, 111, 919
- Hogg, D. W., Finkbeiner, D. P., Schlegel, D. J., & Gunn, J. E. 2001, *AJ*, 122, 2129
- Israelian, F., Ecuivillon, A., Rebolo, R., et al. 2004, *A&A*, 421, 649
- Izotov, Y.I., Stasinsda, G., Meyenet, G., Guseva, N. G., & Thuan, T. X. 2006, *A&A*, 448, 955
- Kauffmann, F. et al. 2003, *MNRAS*, 341,33
- Kauffmann, G. et al. 2003, *MNRAS*, 346, 1055
- Kennicutt, R. C., Bresolin, F., & Garnett, D. R. 2003, *ApJ*, 591, 801
- Kewley, L. J., Jansen R. A., & Geller, M. J. 2005, *PASP* 117, 227
- Kewley, L. J., & Dopita, M. A. 2002, *ApJS*, 142, 35
- Kewley, L. J., Dopita, M. A., Sutherland, R. S., Heisler, C. A., & Trevena, J. 2001, *ApJ*, 556,121
- Kobulnicky, H. A., Kennicutt, & R. C, Pizagno, J. L. 1999, *ApJ*, 514, 544
- Kroupa P., 2001, *MNRAS*, 322,231
- Linag, Y. C., Yin, S. Y., Hammer, F., Deng, L., C., Flores, H., & Zhang, B. 2006, *ApJ*, 652, 257
- Maeder, A. 2000, *New Astronomy Review*, 44, 291
- Martin, C. D. et al. 2008 this volume
- Matteucci, F. 1986, *MNRAS*, 221 911
- Matteucci, F., Tornambe, A. 1985, *A&A*, 142, 13
- Matteucci, F., & Tosi, M. 1985, *MNRAS* 217 391
- McGaugh, S. S. 1991, *ApJ*, 380, 140
- Milliard B., Donas J., Laget M., Armand C., Vuillemin A. 1992, *A&A*, 257, 24
- Morrissey, P. et al. 2008, this volume
- Oey, M. S., Dopita, M. A., Shields, J. C., Smith, R. C. 2000, *ApJS*, 128, 511
- Osterbrock, D. E. 1989, *Astrophysics of Gaseous Nebulae and Active Galactic Nuclei* (Mill Valley:University Science Books)
- Pagel, B. E. J., Edmonds, M. G., Blackwell, D. E., Chun, M. S., & Smith, G. 1979, *MNRAS*, 189, 95
- Pagel, B. E. J., Simonson, E. A., Terlevich, R. J., & Edmunds, M. G. 1992, *MNRAS* 255 325
- Peimbert, M., Peimbert, A., Esteban, C., Garcia-Rojas, J., Bresolin, F., Carigi, L., Ruiz, M.T., & Lopez-Sanchez, A.R. 2006, *RevMexAA*, in press
- Pettini, M., Steidel, C. C., Adelberger, D. L., & Giavalisco, M. 2001, *ApJ*, 528, 96
- Pettini, M., & Pagel, B. E. J. 2004, *MNRAS*, 348, 59
- Pier, J. R., Munn, J. A., Hindsley, R. B., Hennessy, G. S., Kent, S. M., Lupton, R. H., & Ivezić, Z. 2003, 125, 1559
- Salim, S. et al. 2005, *ApJ*, 619, 39
- Salim, S. et al. 2008, this volume
- Scully, S., Casse, M., Olive, K. A., & Vangioni-Flam, E. 1996, *ApJ*, 462, 960
- Seaton, M. J. 1979, *MNRAS* 187, 785
- Seibert, M. et al. 2005, *ApJ*, 619, 23
- Shaw, R. A., & Dufour, R. J. 1995, *PASP*, 107, 896
- Silk, J. 1995, *ApJ*, 438, L41
- Smith, J. A. et al. 2002, *AJ*, 123, 2121
- Spite, M., Cayrel, R., Plez, B., et al. 2005, *A&A*, 430, 655 (S05)
- Stasinka, G. 1990, *A&AS*, 83, 501
- Stoughton, C. et al. 2002, *AJ*, 123, 485
- Bower, R. G. 2001, *MNRAS*, 326, 1547
- Thurston, T. R., Edmunds, M. G., Henry, R. B. C. 1996, *MNRAS*, 283, 990
- Tremonti, C. A. et al. 2004, *ApJ*, 613, 898
- van Zee, L., & Haynes, M. P. 2006, *ApJ*, 636, 214
- Vila-Costas, M. V. & Edmunds M. G. 1992, *MNRAS*, 265, 199
- Woolsey, S. E., & Weaver, T. A. 1995, *ApJS*, 101, 181
- York, D. G., Adelman, J., Anderson, J. E., Jr., et al. 2000, *AJ*, 120, 1579

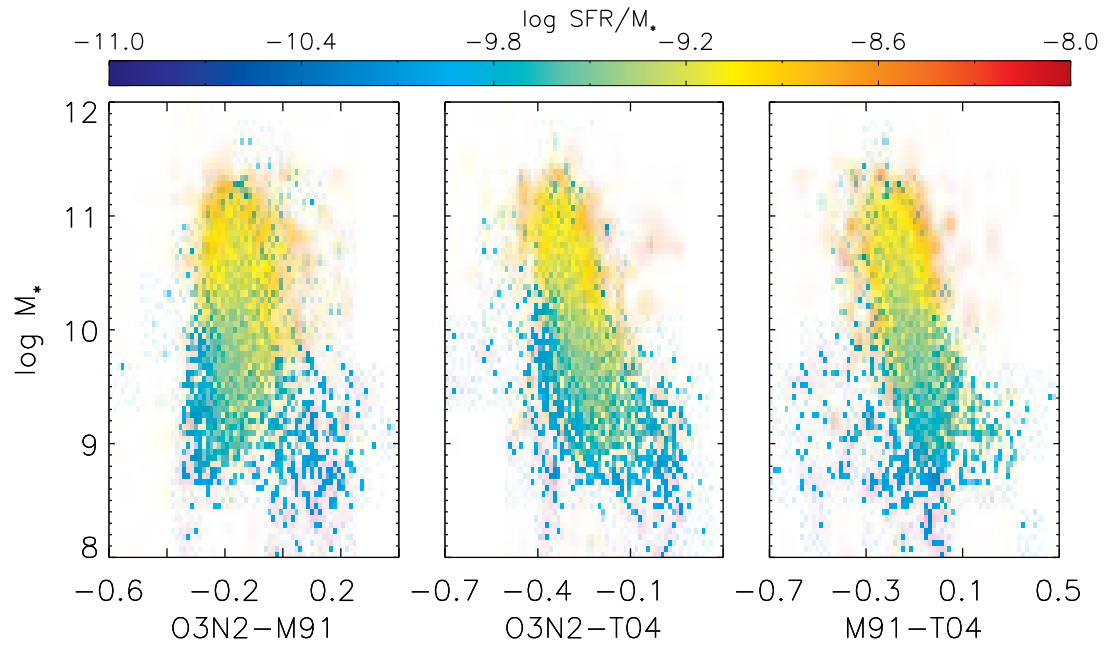


FIG. 1.— Comparison of abundances from three different diagnostics: O3N2, M91, and T04 as a function of stellar mass. The data points are converted into a 75 by 75 pixel image. The mean specific SFR value of the points in each pixel is calculated and byte-scaled into true color. The difference between T04 and the other two diagnostics shows a dependence on mass since T04 estimates an increasingly larger metallicity at higher stellar masses.

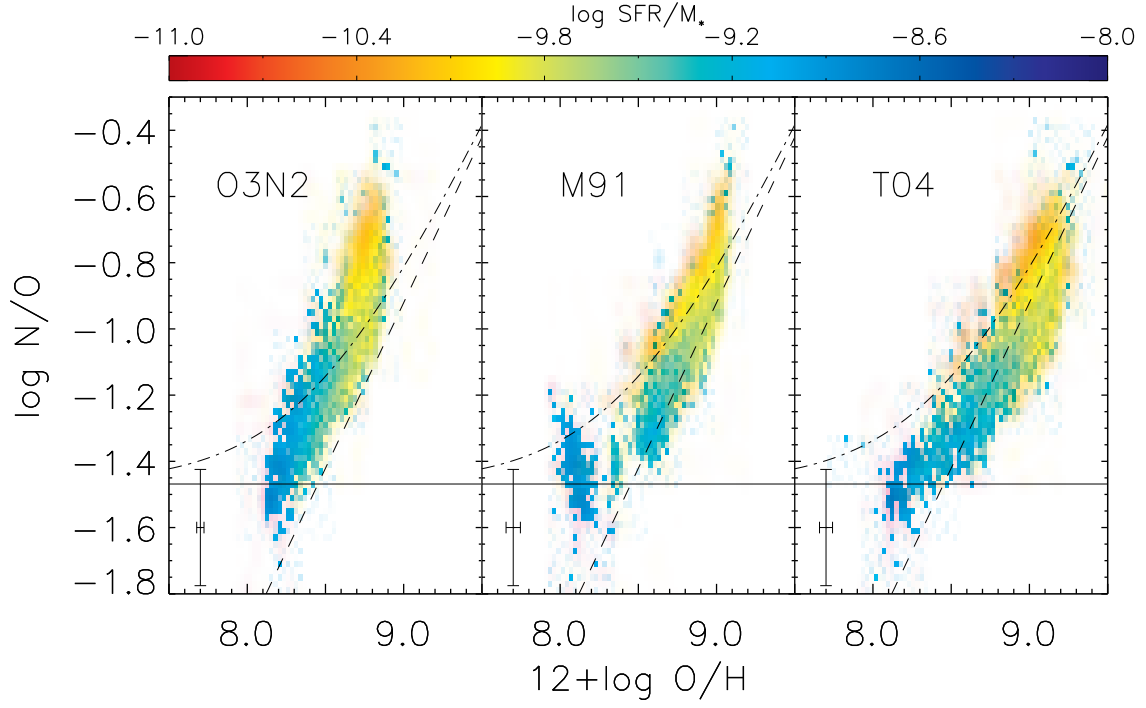


FIG. 2.—  $N/O$  versus  $O/H$  for three different methods of abundance determination. The points are binned into a 75 by 75 pixel image, with the mean value of specific star formation rate ( $SFR/M_*$ ) calculated from the points in each pixel and byte scaled into a true color representation. The specific star formation rate is an indicator of the star formation history of the galaxy. The plot shows the general trend that galaxies with similar metallicities have lower  $N/O$  ratios for larger values of  $SFR/M_*$ . This trend supports the time delay scenario where the the bulk of the oxygen is released from short lived massive stars, and the release of the bulk of the nitrogen from longer lived intermediate mass stars.

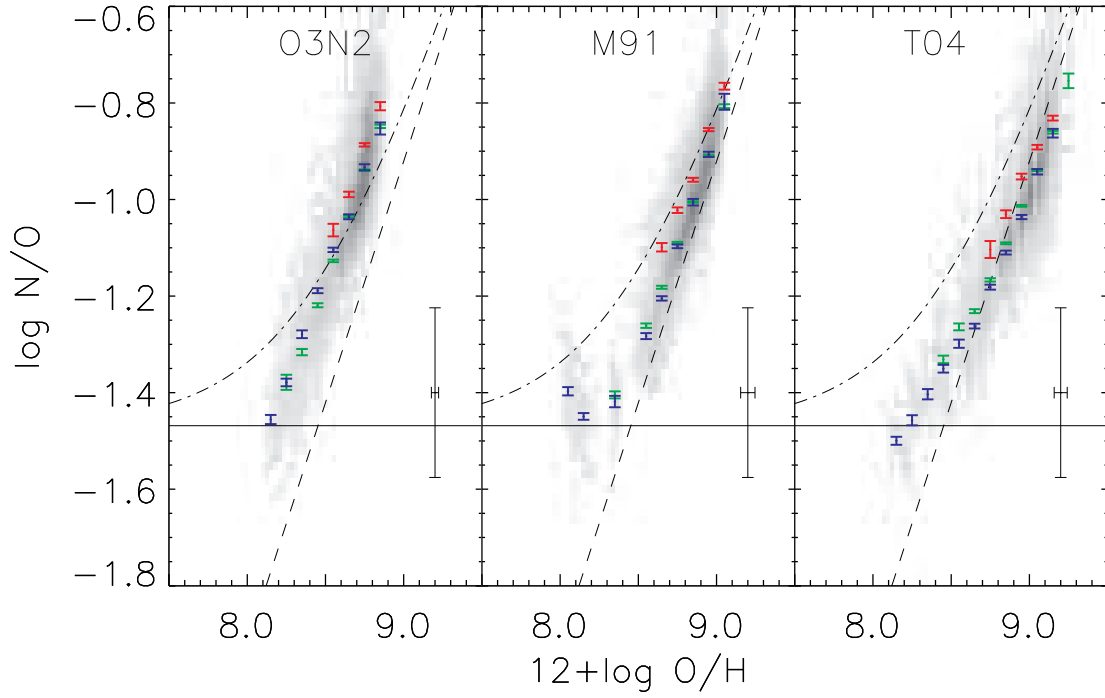


FIG. 3.— 2D Histogram of N/O versus O/H. The red points represent the mean N/O values for objects with  $\text{SFR}/M_* < -10.1$  taken for metallicity increments of 0.1 dex. The green points represent objects with  $-10.1 < \text{SFR}/M_* < -9.1$ , and the blue data points represent galaxies with  $\text{SFR}/M_* > -9.1$ . The abundance methods of O3N2, M91 and T04 all show that the starbursts (having values of  $\text{SFR}/M_* > -10.1$ ) have lower values of N/O than galaxies of similar metallicity that are currently not forming as large a fraction of their stellar mass.

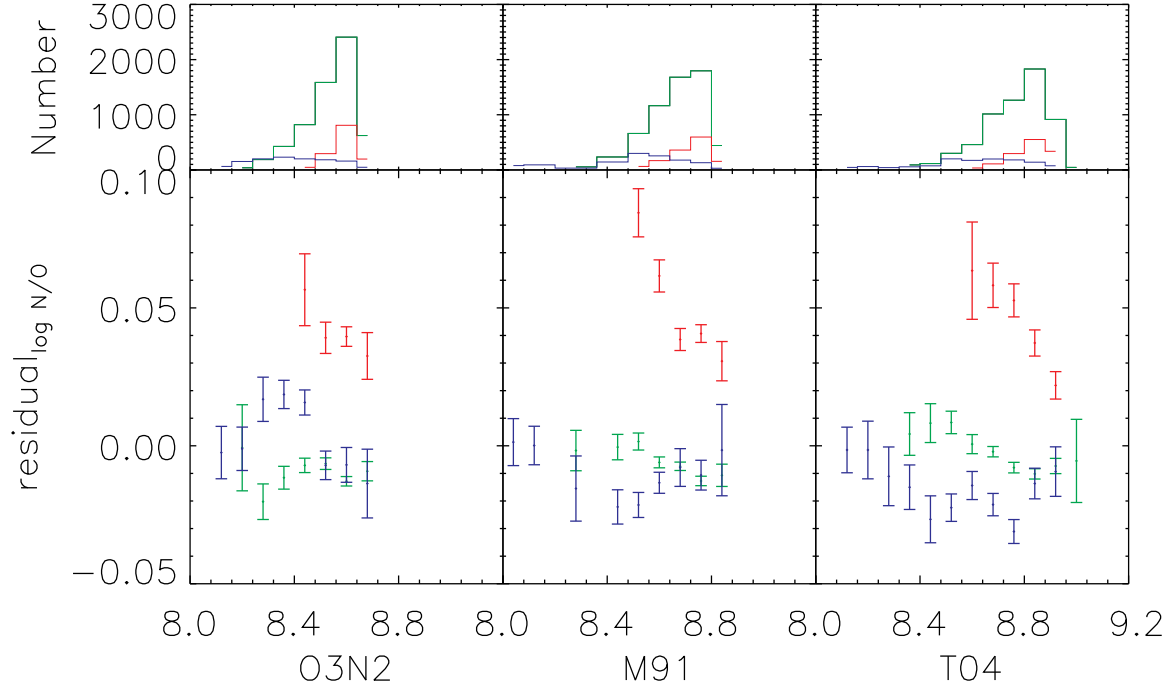


FIG. 4.— Difference of mean N/O ratios between three sub-samples of specific star formation rate and the mean N/O of the entire sub-sample taken for metallicity increments of 0.1dex. The red points represent the mean N/O values for objects with  $SFR/M_* < -10.1$ , the green points represent objects with  $-10.1 < SFR/M_* < -9.1$ , and the blue data points represent galaxies with  $SFR/M_* > -9.1$ . The abundance methods of O3N2, M91 and T04 all show that galaxies with the lowest specific star formation rates (having values of  $SFR/M_* < -10.1$ ) have higher values of N/O than galaxies of similar metallicity with  $\log SFR/M_* > -10.1$ . At intermediate metallicities the most extreme starbursts ( $\log SFR/M_* > -9.1$ ) on average have slightly lower N/O ratios than galaxies with average specific star formation rates ( $-10.1 < \log SFR/M_* < -9.1$ ) by 0.02 dex presumably due to oxygen released by the high mass stars formed in the starburst

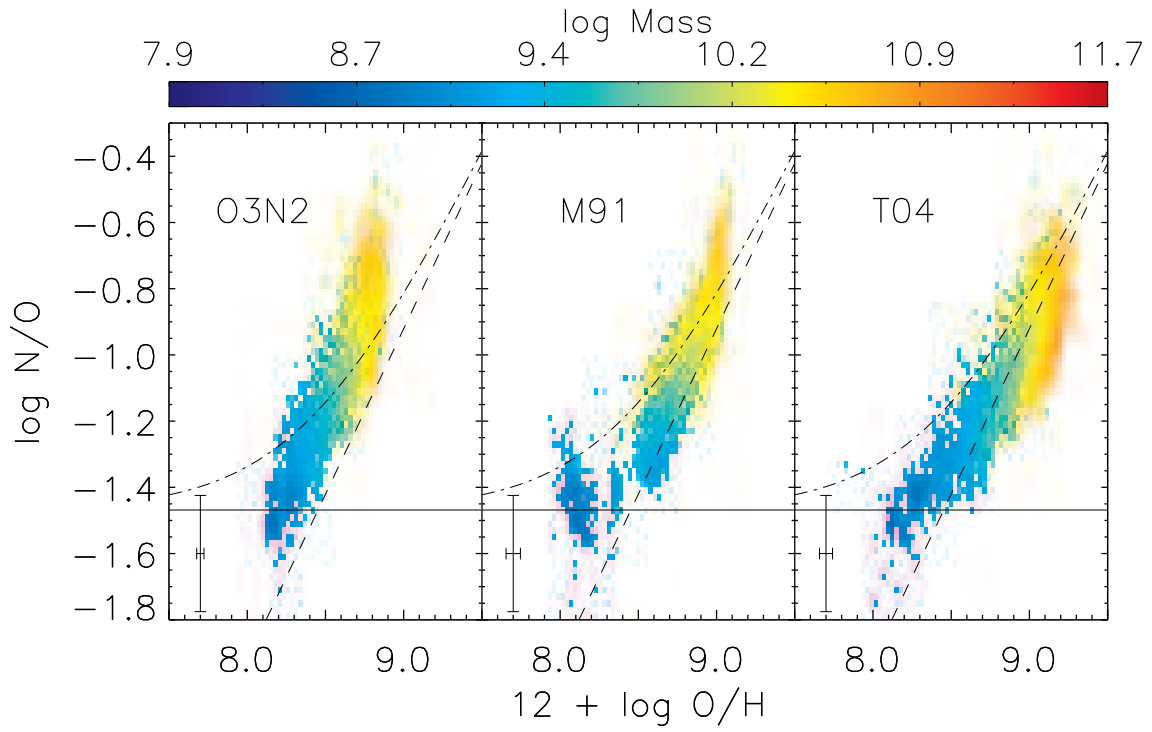


FIG. 5.—  $N/O$  versus  $O/H$  scaled with  $\text{Log } M_*$ . This shows that  $M_*$  increases with increasing metallicity, and tends to have little dependence on  $N/O$  at a given metallicity.

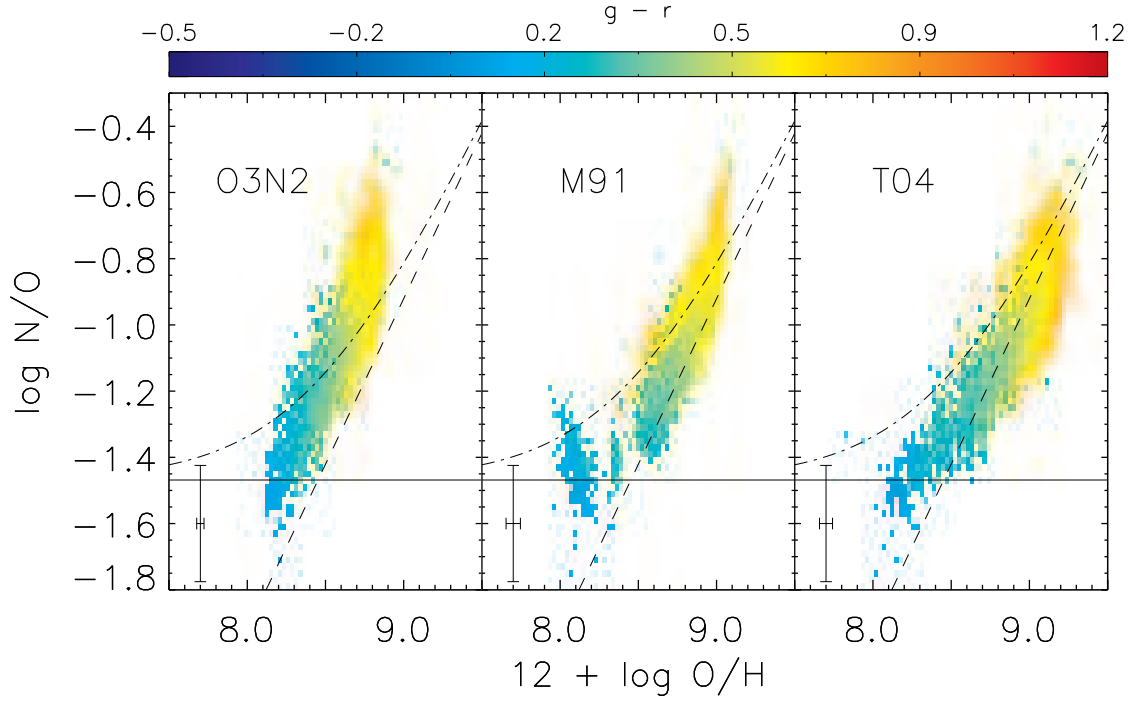


FIG. 6.—  $N/O$  versus  $O/H$ , scaled with  $g-r$ . This plot shows that the  $g-r$  color of galaxies is redder for galaxies with higher metallicities. Also for galaxies with similar metallicities, those galaxies with larger values of  $N/O$  have a redder color. This is because redder galaxies have increasingly declining SFRs, where the intermediate mass stars from previous star formation events have released nitrogen into the ISM. This confirms the result of van Zee & Haynes (2006) who found a similar trend for dwarf galaxies.

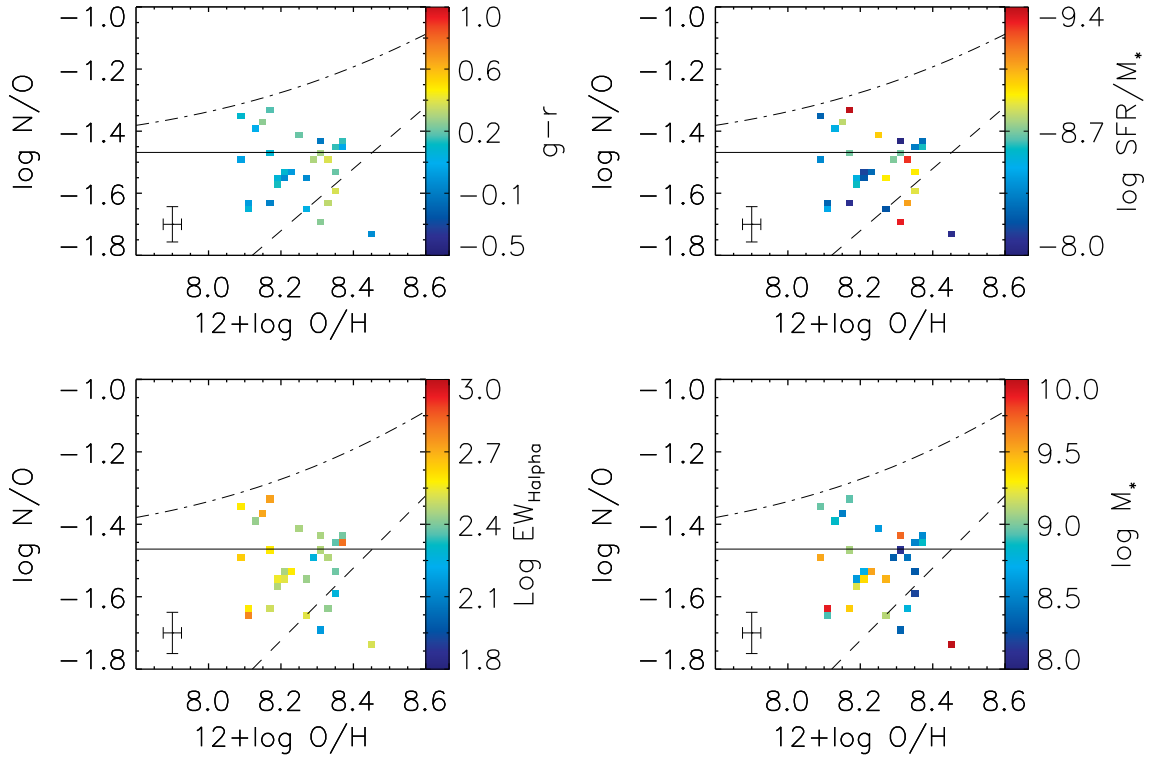


FIG. 7.— N/O versus O/H for abundances calculated using the  $T_e$  method. Overall the galaxies with  $\log N/O < -1.5$  on average tend to be slightly bluer, with higher equivalent widths, and with specific star formation rates 0.12 dex higher than galaxies with  $\log N/O > -1.5$ . The  $T_e$  oxygen abundances show little correlation with stellar mass, but this is probably due to small sample size and errors in the derived abundances. A larger sample size of galaxies with abundances derived from the  $T_e$  method with a greater range of equivalent widths, stellar masses, and specific star formation rates, are needed to confirm the results from O3N2, M91, and T04.



TABLE 1  
AVERAGE GALAXY PARAMETER ERRORS

Parameter	$\langle value \rangle$	$\langle \sigma \rangle$
$\log M_*$	10.10	0.075
$\langle \log SFR \rangle_{100Myr}$	0.48	0.20
$\langle \log SFR/M_* \rangle_{100Myr}$	-9.6	0.19
$\log b$	-0.24	0.22
$A_{FUV}$	2.40	0.56
$A_{NUV}$	1.78	0.43

TABLE 2  
 $T_e$  ABUNDANCES

$\alpha$ J2000	dJ2000	$12 + \log O/H$	$\log N/O$	$\log SFR/M_*$	$M_*$	$F_{BURST}^1$	$g-r$	$\log EW_{H\alpha}$
20 <sup>h</sup> 40 <sup>m</sup> 18.047 <sup>s</sup>	01°03'24".59	8.31 ±0.023	-1.43 ±0.047	-8.19 ±0.087	8.28 ±0.057	0.00 <sup>0.65</sup> <sub>0.00</sub>	-0.13	2.355
20 <sup>h</sup> 52 <sup>m</sup> 51.797 <sup>s</sup>	00°16'26".00	8.16 ±0.028	-1.38 ±0.057	-8.89 ±0.170	9.54 ±0.115	0.10 <sup>0.15</sup> <sub>0.00</sub>	0.31	2.091
21 <sup>h</sup> 18 <sup>m</sup> 29.846 <sup>s</sup>	00°30'59".55	8.18 ±0.017	-1.56 ±0.049	-9.16 ±0.178	9.26 ±0.115	0.00 <sup>0.15</sup> <sub>0.00</sub>	0.39	2.506
22 <sup>h</sup> 07 <sup>m</sup> 07.888 <sup>s</sup>	00°46'58".78	8.10 ±0.030	-1.62 ±0.086	-8.39 ±0.150	8.11 ±0.082	0.00 <sup>0.51</sup> <sub>0.00</sub>	0.00	2.216
22 <sup>h</sup> 12 <sup>m</sup> 23.328 <sup>s</sup>	00°03'39".86	8.24 ±0.031	-1.40 ±0.062	-9.06 ±0.247	9.41 ±0.128	0.05 <sup>0.32</sup> <sub>0.00</sub>	0.26	2.354
21 <sup>h</sup> 50 <sup>m</sup> 29.868 <sup>s</sup>	00°32'01".26	8.24 ±0.032	-1.53 ±0.070	-8.24 ±0.173	8.19 ±0.105	0.00 <sup>0.36</sup> <sub>0.00</sub>	-0.09	2.349
20 <sup>h</sup> 46 <sup>m</sup> 56.140 <sup>s</sup>	00°50'37".63	8.27 ±0.032	-1.66 ±0.070	-8.34 ±0.192	8.90 ±0.140	0.38 <sup>0.93</sup> <sub>0.00</sub>	0.10	2.279
10 <sup>h</sup> 53 <sup>m</sup> 42.546 <sup>s</sup>	00°09'45".13	8.19 ±0.024	-1.55 ±0.053	-8.66 ±0.188	9.41 ±0.113	0.18 <sup>0.47</sup> <sub>0.00</sub>	0.14	2.258
17 <sup>h</sup> 09 <sup>m</sup> 22.632 <sup>s</sup>	61°48'51".25	8.36 ±0.026	-1.45 ±0.048	-8.47 ±0.155	9.52 ±0.118	0.25 <sup>0.67</sup> <sub>0.15</sub>	0.22	2.440
00 <sup>h</sup> 53 <sup>m</sup> 00.523 <sup>s</sup>	15°01'29".73	8.19 ±0.021	-1.58 ±0.047	-8.28 ±0.153	8.36 ±0.062	0.00 <sup>0.77</sup> <sub>0.00</sub>	0.00	2.183
08 <sup>h</sup> 01 <sup>m</sup> 43.632 <sup>s</sup>	44°54'58".41	8.37 ±0.025	-1.46 ±0.052	-8.73 ±0.092	9.16 ±0.085	0.10 <sup>0.24</sup> <sub>0.00</sub>	0.04	1.985
08 <sup>h</sup> 20 <sup>m</sup> 01.714 <sup>s</sup>	50°50'39".20	8.35 ±0.020	-1.59 ±0.045	-8.94 ±0.120	9.82 ±0.053	0.00 <sup>0.14</sup> <sub>0.00</sub>	0.43	2.537
08 <sup>h</sup> 47 <sup>m</sup> 03.007 <sup>s</sup>	54°50'39".45	8.22 ±0.019	-1.53 ±0.060	-8.30 ±0.162	9.28 ±0.125	0.41 <sup>0.43</sup> <sub>0.00</sub>	0.15	2.356
03 <sup>h</sup> 05 <sup>m</sup> 39.705 <sup>s</sup>	-08°39'05".24	8.20 ±0.027	-1.55 ±0.083	-8.36 ±0.163	8.65 ±0.092	0.10 <sup>0.99</sup> <sub>0.00</sub>	-0.06	2.279
12 <sup>h</sup> 05 <sup>m</sup> 14.725 <sup>s</sup>	66°16'57".80	8.32 ±0.030	-1.50 ±0.058	-9.34 ±0.072	9.61 ±0.047	0.00 <sup>0.03</sup> <sub>0.00</sub>	0.44	2.346
10 <sup>h</sup> 23 <sup>m</sup> 19.567 <sup>s</sup>	02°49'41".53	8.08 ±0.031	-1.35 ±0.059	-8.39 ±0.243	9.05 ±0.140	0.05 <sup>0.31</sup> <sub>0.00</sub>	0.16	2.218
11 <sup>h</sup> 36 <sup>m</sup> 55.796 <sup>s</sup>	03°33'33".40	8.34 ±0.024	-1.54 ±0.047	-9.00 ±0.158	9.73 ±0.117	0.06 <sup>0.19</sup> <sub>0.00</sub>	0.26	2.422
08 <sup>h</sup> 39 <sup>m</sup> 14.949 <sup>s</sup>	48°15'18".24	8.17 ±0.027	-1.47 ±0.053	-8.51 ±0.217	8.49 ±0.112	0.00 <sup>0.37</sup> <sub>0.00</sub>	0.13	2.136
09 <sup>h</sup> 46 <sup>m</sup> 30.590 <sup>s</sup>	55°35'41".81	8.23 ±0.031	-1.53 ±0.062	-8.58 ±0.140	8.76 ±0.075	0.00 <sup>0.21</sup> <sub>0.00</sub>	0.08	2.084
14 <sup>h</sup> 05 <sup>m</sup> 01.154 <sup>s</sup>	04°31'26".13	8.46 ±0.027	-1.74 ±0.054	-8.23 ±0.105	8.00 ±0.035	0.00 <sup>0.65</sup> <sub>0.00</sub>	-0.06	2.297
14 <sup>h</sup> 36 <sup>m</sup> 48.204 <sup>s</sup>	04°02'59".92	8.17 ±0.031	-1.34 ±0.060	-9.44 ±0.070	9.06 ±0.082	0.00 <sup>0.02</sup> <sub>0.00</sub>	0.23	2.077
14 <sup>h</sup> 46 <sup>m</sup> 10.316 <sup>s</sup>	03°39'21".55	8.31 ±0.016	-1.46 ±0.032	-8.71 ±0.162	9.75 ±0.100	0.16 <sup>0.26</sup> <sub>0.06</sub>	0.28	2.437
14 <sup>h</sup> 54 <sup>m</sup> 24.609 <sup>s</sup>	03°59'25".20	8.29 ±0.020	-1.49 ±0.041	-8.81 ±0.185	9.71 ±0.075	0.00 <sup>0.47</sup> <sub>0.00</sub>	0.36	2.543
00 <sup>h</sup> 52 <sup>m</sup> 49.794 <sup>s</sup>	-08°41'33".93	8.10 ±0.034	-1.49 ±0.070	-8.51 ±0.202	8.48 ±0.145	0.00 <sup>0.46</sup> <sub>0.00</sub>	0.02	2.163
01 <sup>h</sup> 38 <sup>m</sup> 44.917 <sup>s</sup>	-08°35'40".69	8.18 ±0.017	-1.62 ±0.045	-8.24 ±0.235	8.60 ±0.033	0.42 <sup>0.68</sup> <sub>0.00</sub>	-0.09	2.303
01 <sup>h</sup> 47 <sup>m</sup> 21.680 <sup>s</sup>	-09°16'46".23	8.31 ±0.018	-1.70 ±0.050	-9.37 ±0.145	9.68 ±0.115	0.03 <sup>0.12</sup> <sub>0.02</sub>	0.30	2.642
02 <sup>h</sup> 03 <sup>m</sup> 56.913 <sup>s</sup>	-08°07'58".48	8.37 ±0.018	-1.43 ±0.036	-8.43 ±0.162	9.48 ±0.090	0.25 <sup>0.52</sup> <sub>0.00</sub>	0.21	2.414
22 <sup>h</sup> 58 <sup>m</sup> 33.743 <sup>s</sup>	00°56'30".53	8.13 ±0.032	-1.39 ±0.081	-8.65 ±0.270	9.17 ±0.193	0.17 <sup>0.99</sup> <sub>0.00</sub>	0.08	2.377
23 <sup>h</sup> 29 <sup>m</sup> 32.117 <sup>s</sup>	00°34'26".91	8.32 ±0.029	-1.63 ±0.079	-9.15 ±0.065	9.23 ±0.100	0.00 <sup>0.06</sup> <sub>0.00</sub>	0.39	2.382
22 <sup>h</sup> 53 <sup>m</sup> 56.829 <sup>s</sup>	10°13'00".29	8.31 ±0.031	-1.46 ±0.060	-8.88 ±0.092	10.04 ±0.108	0.10 <sup>0.10</sup> <sub>0.00</sub>	0.41	2.252
10 <sup>h</sup> 21 <sup>m</sup> 32.505 <sup>s</sup>	61°44'04".52	8.16 ±0.023	-1.48 ±0.056	-9.08 ±0.207	9.36 ±0.123	0.06 <sup>0.22</sup> <sub>0.00</sub>	0.16	2.294
08 <sup>h</sup> 20 <sup>m</sup> 10.558 <sup>s</sup>	37°43'54".34	8.11 ±0.026	-1.66 ±0.060	-8.60 ±0.162	9.09 ±0.077	0.00 <sup>0.38</sup> <sub>0.00</sub>	0.13	2.022
21 <sup>h</sup> 19 <sup>m</sup> 58.308 <sup>s</sup>	00°52'33".52	8.26 ±0.016	-1.55 ±0.046	-9.00 ±0.435	8.52 ±0.015	0.07 <sup>0.00</sup> <sub>0.00</sub>	-0.06	2.375

<sup>1</sup> The superscripts for  $F_{BURST}$  (Fraction of stellar mass formed in starbursts over the last 100Myr) list the 97.5 percentile values, and the subscripts list the 2.5 percentile values.

<sup>1</sup> Sub-sample a: galaxies with  $SFR/M_* < -10.1$ , Sub-sample b: galaxies with  $-10.1 < SFR/M_* < -9.1$ , Sub-sample c galaxies with  $SFR/M_* > -9.1$

TABLE 3  
O3N2 MEAN N/O

$12 + \log O/H$	Sub-sample <sup>1</sup>	#of galaxies	$\log N/O_{mean}$	$\log SFR/M_{*mean}$	$\log M_{*mean}$	$g - r_{mean}$
8.55	a	47	$-1.06 \pm 0.013$	$-10.49 \pm 0.055$	$10.14 \pm 0.081$	$0.69 \pm 0.023$
	b	873	$-1.13 \pm 0.003$	$-9.49 \pm 0.008$	$9.74 \pm 0.011$	$0.43 \pm 0.003$
	c	149	$-1.10 \pm 0.005$	$-8.88 \pm 0.018$	$9.88 \pm 0.029$	$0.36 \pm 0.007$
8.65	a	295	$-0.99 \pm 0.006$	$-10.34 \pm 0.014$	$10.27 \pm 0.025$	$0.71 \pm 0.006$
	b	1638	$-1.04 \pm 0.002$	$-9.62 \pm 0.006$	$10.05 \pm 0.009$	$0.52 \pm 0.002$
	c	132	$-1.04 \pm 0.006$	$-8.89 \pm 0.020$	$10.06 \pm 0.028$	$0.43 \pm 0.008$
8.75	a	809	$-0.89 \pm 0.004$	$-10.33 \pm 0.008$	$10.53 \pm 0.013$	$0.74 \pm 0.004$
	b	2459	$-0.94 \pm 0.002$	$-9.71 \pm 0.005$	$10.38 \pm 0.007$	$0.60 \pm 0.002$
	c	109	$-0.93 \pm 0.008$	$-8.88 \pm 0.024$	$10.48 \pm 0.034$	$0.55 \pm 0.011$
8.85	a	197	$-0.81 \pm 0.008$	$-10.34 \pm 0.021$	$10.58 \pm 0.023$	$0.74 \pm 0.007$
	b	637	$-0.85 \pm 0.003$	$-9.68 \pm 0.009$	$10.50 \pm 0.014$	$0.63 \pm 0.004$
	c	36	$-0.85 \pm 0.015$	$-8.92 \pm 0.030$	$10.48 \pm 0.050$	$0.59 \pm 0.015$

<sup>1</sup> Sub-sample a: galaxies with  $SFR/M_* < -10.1$ , Sub-sample b: galaxies with  $-10.1 < SFR/M_* < -9.1$ , Sub-sample c: galaxies with  $SFR/M_* > -9.1$

TABLE 4  
M91 MEAN N/O

$12 + \log O/H$	Sub-sample <sup>1</sup>	#of galaxies	$\log N/O_{mean}$	$\log SFR/M_{*mean}$	$\log M_{*mean}$	$g - r_{mean}$
8.65	a	64	$-1.10 \pm 0.009$	$-10.48 \pm 0.044$	$10.12 \pm 0.085$	$0.69 \pm 0.024$
	b	733	$-1.18 \pm 0.003$	$-9.47 \pm 0.009$	$9.62 \pm 0.017$	$0.42 \pm 0.004$
	c	229	$-1.21 \pm 0.005$	$-8.85 \pm 0.016$	$9.58 \pm 0.030$	$0.31 \pm 0.007$
8.75	a	169	$-1.02 \pm 0.006$	$-10.40 \pm 0.024$	$10.27 \pm 0.036$	$0.71 \pm 0.009$
	b	1228	$-1.09 \pm 0.002$	$-9.55 \pm 0.007$	$9.92 \pm 0.012$	$0.48 \pm 0.004$
	c	191	$-1.10 \pm 0.004$	$-8.88 \pm 0.016$	$9.92 \pm 0.027$	$0.37 \pm 0.008$
8.85	a	360	$-0.96 \pm 0.004$	$-10.33 \pm 0.011$	$10.37 \pm 0.023$	$0.72 \pm 0.005$
	b	1733	$-1.01 \pm 0.001$	$-9.64 \pm 0.006$	$10.17 \pm 0.010$	$0.55 \pm 0.003$
	c	126	$-1.00 \pm 0.009$	$-8.84 \pm 0.024$	$10.13 \pm 0.041$	$0.46 \pm 0.010$
8.95	a	597	$-0.86 \pm 0.003$	$-10.33 \pm 0.009$	$10.55 \pm 0.015$	$0.74 \pm 0.004$
	b	1839	$-0.91 \pm 0.002$	$-9.70 \pm 0.006$	$10.39 \pm 0.009$	$0.60 \pm 0.002$
	c	89	$-0.91 \pm 0.007$	$-8.89 \pm 0.024$	$10.38 \pm 0.041$	$0.53 \pm 0.012$

TABLE 5  
T04 MEAN N/O

$12 + \log O/H$	Sub-sample <sup>1</sup>	#of galaxies	$\log N/O_{mean}$	$\log M_{*mean}$	$\log L_{FUV}/M_{*mean}$	$g - r_{mean}$
8.75	a	35	$-1.10 \pm 0.018$	$-10.38 \pm 0.045$	$9.96 \pm 0.102$	$0.64 \pm 0.028$
	b	506	$-1.17 \pm 0.003$	$-9.47 \pm 0.010$	$9.63 \pm 0.014$	$0.42 \pm 0.004$
	c	128	$-1.18 \pm 0.006$	$-8.85 \pm 0.021$	$9.67 \pm 0.029$	$0.32 \pm 0.008$
8.85	a	110	$-1.03 \pm 0.008$	$-10.41 \pm 0.032$	$10.03 \pm 0.042$	$0.67 \pm 0.011$
	b	1060	$-1.09 \pm 0.002$	$-9.55 \pm 0.007$	$9.84 \pm 0.010$	$0.47 \pm 0.003$
	c	154	$-1.11 \pm 0.005$	$-8.86 \pm 0.019$	$9.90 \pm 0.027$	$0.37 \pm 0.008$
8.95	a	297	$-0.95 \pm 0.006$	$-10.34 \pm 0.013$	$10.31 \pm 0.022$	$0.71 \pm 0.006$
	b	1313	$-1.01 \pm 0.002$	$-9.63 \pm 0.007$	$10.10 \pm 0.009$	$0.53 \pm 0.003$
	c	133	$-1.04 \pm 0.005$	$-8.86 \pm 0.022$	$10.06 \pm 0.033$	$0.42 \pm 0.009$
9.05	a	551	$-0.89 \pm 0.005$	$-10.32 \pm 0.009$	$10.51 \pm 0.015$	$0.74 \pm 0.004$
	b	1874	$-0.94 \pm 0.002$	$-9.70 \pm 0.006$	$10.37 \pm 0.008$	$0.59 \pm 0.002$
	c	95	$-0.95 \pm 0.006$	$-8.87 \pm 0.027$	$10.36 \pm 0.036$	$0.51 \pm 0.011$
9.15	a	338	$-0.83 \pm 0.005$	$-10.35 \pm 0.015$	$10.68 \pm 0.017$	$0.76 \pm 0.005$
	b	935	$-0.86 \pm 0.003$	$-9.71 \pm 0.008$	$10.60 \pm 0.011$	$0.65 \pm 0.003$
	c	56	$-0.86 \pm 0.011$	$-8.93 \pm 0.024$	$10.59 \pm 0.043$	$0.60 \pm 0.015$

<sup>1</sup> Sub-sample a: galaxies with  $SFR/M_* < -10.1$ , Sub-sample b: galaxies with  $-10.1 < SFR/M_* < -9.1$ , Sub-sample c: galaxies with  $SFR/M_* > -9.1$